ELSEVIER

Journal of Quantitative Spectroscopy & Radiative Transfer 99 (2006) 712–729

Journal of Quantitative Spectroscopy & Radiative Transfer

www.elsevier.com/locate/jqsrt

Study of X-ray photoionized Fe plasma and comparisons with astrophysical modeling codes

M.E. Foord[a,*], R.F. Heeter[a], H.-K. Chung[a], P.A.M. van Hoof[c], J.E. Bailey[b], M.E. Cuneo[b], D.A. Liedahl[a], K.B. Fournier[a], V. Jonauskas[c], R. Kisielius[c], C. Ramsbottom[c], P.T. Springer[a], F.P. Keenan[c], S.J. Rose[d], W.H. Goldstein[a]

[a]*Lawrence Livermore National Laboratory, Livermore, CA 94551, USA*
[b]*Sandia National Laboratory, Albuquerque, NM, 37185, USA*
[c]*Department of Pure and Applied Physics, Queen's University Belfast, BT7 1NN, N. Ireland, UK*
[d]*Department of Physics, Clarendon Laboratory, Parks Road, Oxford OX1 3PU, UK*

Accepted 26 April 2005

Abstract

The charge state distributions of Fe, Na and F are determined in a photoionized laboratory plasma using high-resolution X-ray spectroscopy. Independent measurements of the density and radiation flux indicate the ionization parameter ξ in the plasma reaches values $\xi = 20-25\,\mathrm{erg\,cm\,s^{-1}}$ under near steady-state conditions. A curve-of-growth analysis, which includes the effects of velocity gradients in a one-dimensional expanding plasma, fits the observed line opacities. Absorption lines are tabulated in the wavelength region 8–17 Å. Initial comparisons with a number of astrophysical X-ray photoionization models show reasonable agreement.

Keywords: Plasma spectroscopy; Astrophysical observation; X-ray spectra; Population kinetics

*Corresponding author. Tel.: +1 925 422 0990.
E-mail address: foord1@llnl.gov (M.E. Foord).

0022-4073/$ - see front matter © 2005 Published by Elsevier Ltd.
doi:10.1016/j.jqsrt.2005.05.057

1. Introduction

Accretion-driven binary stars and active galactic nuclei (AGN) are among the strongest X-ray sources in the universe. For the first time, recently launched X-ray observatories, XMM-Newton and Chandra are recording high-resolution spectral data from these powerful radiators [1,2]. The complex emission and absorption spectra from such objects provide important clues to their structure and dynamics, such as their charge state distributions and velocity flows. It is therefore of interest, and the purpose of this work, to simulate in the laboratory the strong photoionizing environment found near these bright X-ray sources, and to use these data to directly test and improve spectroscopic models and photoionization codes that are applied to their analysis.

Recent Chandra data from the NGC3783 galaxy illustrates the difficulties involved in interpreting well-resolved astrophysical spectra. From its X-ray signature, NGC3783 is classified as a Seyfert I galaxy. It is thought that Seyfert galaxies consist of a torus of stars and gas that encircle a massive black hole. Thermal and non-thermal X-ray radiation produced near the galaxy center is generated by the inward spiral motion of infalling matter that forms a small disc around the black hole. This powerful X-ray source then photoionizes the surrounding gas. Thus, the absorption spectra of the escaping X-rays, viewed along the toroidal axis, reflects details about the composition and ionization of the surrounding photoionized plasma. In the case of NGC3783, absorption features have been identified with O, Si, and Fe ions at different stages of ionization. The difficulty has been in forming a consistent picture of the distribution of mass that agrees with the ionization states predicted by photoionization codes. A multishell distribution of ions has been proposed by Netzer et al. [3], while a 2-phase model of cold and hot regions has also been suggested by Krongold et al. [4]. Fundamental to the discussion is the photoionization model; the former relies on the code ION2003, which is a more recent version of XION [5], and the latter on the photoionization code Cloudy [6]. Differences in the models are due to the treatment of the atomic rates and the complexity of the levels included in each code. For example, dielectronic recombination, which can be very difficult to include explicitly in the rate equations, may play an important role in determining the ionization balance and cooling rates of Fe [3,7,8].

Many decades of experimental work have provided the high-quality atomic data needed in astrophysics and plasma fusion research. For example, electron-beam ion traps [9], storage rings [10], and tokamaks [11] typically provide measurements of cross-sections, line positions and line strengths needed in spectral synthesis codes. Experiments in higher density collision dominated plasmas have also been used to benchmark ionization models and opacity codes [12–15]. However, until recently [16–21], it has not been possible to create an appropriate environment to test photoionization models, which requires producing a strongly photoionized, low density, near steady-state plasma.

As described below, using a high-power z-pinch X-ray source, photoionized Fe–Na–F plasmas are investigated. High-resolution X-ray spectroscopy and other X-ray diagnostics are used to determine independently the charge state distributions, the absolute radiation flux from the pinch, and the sample densities. Fe is found to photoionize beyond Ne-like (open L-shell), while Na and F photoionize beyond He-like (open K-shell). This allows the first direct comparisons with photoionization models in the relatively low density ($n_e = 2 \times 10^{19}\,\mathrm{cm}^{-3}$) two-body recombination regime.

2. Experiments

A low density, strongly photoionized plasma was produced by placing a thin tamped foil in close proximity to a high-power imploding wire-array z-pinch. The Sandia National Laboratory Z–facility provided a 20 MA, 100 ns rise time current pulse that couples into a 2 cm diameter, 1 cm length wire array, consisting of 300 tightly stretched 11.5 μm diameter tungsten wires. The electromagnetic force implodes the wires onto the central axis, creating a 8 ns FWHM, 120 TW, 165 eV near-blackbody radiation source. An absolutely calibrated transmission grating spectrometer (TGS) measures the spectral and temporal emission from the pinch [22] (see Fig. 1). The pinch emission provides sufficient flux at photon energies above 1 keV to photoionize iron into the L-shell, and also produces a relatively line-free quasi-continuum source of X-ray radiation in the 9–17 Å wavelength range as needed for the absorption experiments described below [16,18–21]. Also shown in Fig. 1 are comparisons with filtered X-ray detectors (XRDs) [23] which show reasonable agreement over most of the energy range. Above 2 keV, spectra were measured using filtered photoconducting detectors (PCDs) [24]. The results presented below were found to be relatively insensitive to the small high-energy component above 2 keV.

Freestanding thin (500–750 Å) rectangular foils were suspended in frames and positioned 1.5–1.6 cm from the z-axis of the pinch. The foils consisted of a 1.35:1 molar ratio of Fe/NaF and were overcoated on each side with 1000 Å of lexan $(C_{16}H_{14}O_3)_n$ to help maintain uniform conditions during heating and expansion. During the initial 100 ns run-in phase, radiation from the tungsten wire array pre-ionizes the foil, causing the central Fe/NaF portion to expand 1.5–2 mm and to decrease in density by many orders of magnitude. A time-gated filtered X-ray pinhole camera images the Fe/NaF emission region edge-on, thus determining the time history of the average density. When the wires collide on axis, the resulting high power X-ray pulse quickly photoionizes the low-density expanded foil. We note that spatially resolved images of the pinch

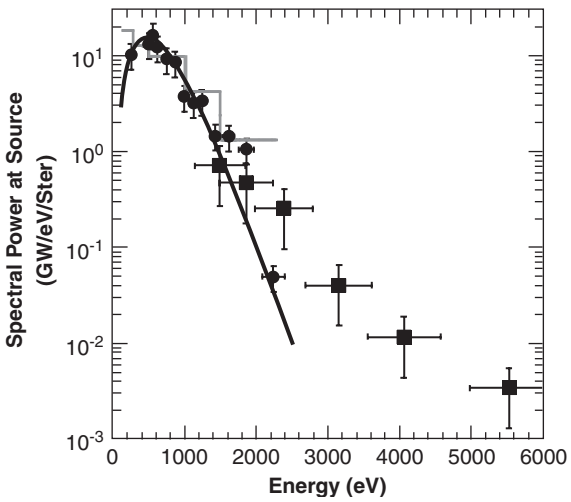

Fig. 1. Z-pinch X-ray spectral emission measured at peak power with an XRD array (stepped lines), a transmission grating spectrometer (dots), and a PCD array (squares). Also shown for comparison is a peak normalized 165 eV blackbody spectrum.

indicate a corrugated cylindrical geometry with multiple hot spots along the length of the pinch. However, since the distance from the foil to the pinch is more than twice the pinch height, and since the hot spots are fairly well distributed along the pinch length, the foil is fairly uniformly illuminated. The inner surface of the can, as well as foil frames and holders, were coated with boron to minimize the re-radiation from nearby surfaces that view the sample. This is important for ensuring that the absolute TGS flux measurement from the pinch is the dominant radiation source for the foils.

In general, at sufficiently low density where two-body processes dominate, the charge state distribution is determined by a balance between photoionization and radiative and dielectronic recombination. In this regime, the degree of ionization can be shown to primarily depend on the ionization parameter $\xi \equiv 16\pi^2 J/n_e$ [25], where J is the mean intensity, $J \equiv (1/4\pi)\int\int J_\nu(\mathbf{\Omega})\,d\mathbf{\Omega}\,d\nu$ integrated over solid angle and integrated in energy from $\chi_H = 13.6\,\text{eV}$ to infinity. ξ is a commonly used scaling parameter in astrophysics which determines the photoionization state in low-density astrophysical plasmas. Far from the radiation source, $\xi \simeq 4\pi\Gamma/n_e$, where $\Gamma(\text{erg cm}^{-2}\,\text{s}^{-1})$ is the incident flux. In these experiments, near the peak of the radiation pulse when $n_e = 2.0 \pm 0.7 \times 10^{19}\,\text{cm}^{-3}$, ξ reaches peak values near $25\,\text{erg cm s}^{-1}$.

3. Simulations

In order to help ensure that the plasma reaches a nearly uniform, steady-state condition near the peak of the radiation pulse, the radiation-hydrodynamics code Lasnex [26] was used to provide guidance on the foil thicknesses and positioning relative to the pinch. These simulations led to the foil dimensions given above, and predicted $\approx \pm 20\%$ variation in the density across the expanded foil. In Fe, the average ionization state, $\langle Z \rangle$, typically varied $\approx \pm 0.3$ across the plasma. Of particular concern was ensuring that the foils expanded sufficiently, both to reach a low-density two-body recombination regime and to allow an accurate density measurement from the filtered emission images, which required $\approx 2\,\text{mm}$ expansion distance. Generally, thicker tamping resulted in better uniformity but at higher densities. Thus, the foil design was a trade-off between reaching a sufficiently low density while maintaining a reasonable uniformity. Simulations predicted that the majority of the foil expansion should occur during the 100 ns run-in phase of the wires, thus ensuring that ion density changed little during the few ns of interest following the peak of the X-ray pulse. Time-resolved filtered X-ray images confirmed these results and were employed to determine an electron density of $n_e = 2.0 \pm 0.7 \times 10^{19}\,\text{cm}^{-3}$, near the peak of the radiation pulse.

4. Theory

The quasi-continuum radiation produced by the pinch is absorbed mainly through bound-free and bound–bound transitions in the plasma and is recorded on film using a time-integrated convex KAP crystal spectrometer. The foil was positioned vertically and expands along the line-of-sight between the pinch and spectrometer. Over the 8.5–17 Å wavelength range the instrumental resolution was $E/\Delta E \simeq 500-800$. Typical absorption data over the 8.5–12 Å

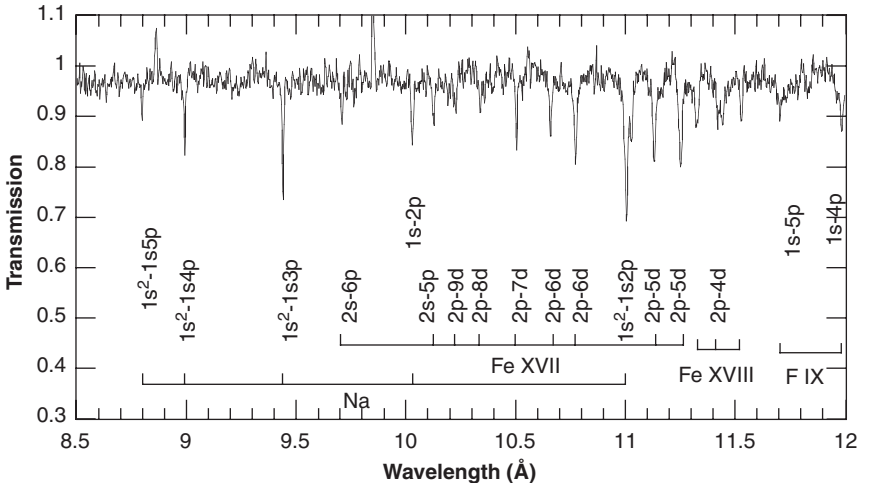

Fig. 2. Absorption spectrum of L-shell iron and K-shell sodium and fluorine lines. Unidentified peaks at 8.8 and 9.8 Å are due to film noise.

portion of the spectrum are shown in Fig. 2, where K-shell absorption lines for Na and F ions, and L-shell absorption lines for Fe are observed. The instrument was arranged to integrate along the length of the pinch, in order to integrate over the spatial variations of the pinch emission.

The Na and F absorption lines were analyzed using a simple one-dimensional expansion model. As discussed above, hydrodynamic simulations indicate that during the initial heating and expansion phase, the central Fe/NaF portion of the foil remains fairly uniform due to the tamping effect of the lexan overcoat. The velocity profile is well approximated by the linear self-similar form $u(x) = u_0(x/x_0)$, where u_0 and x_0 are the velocity and position at the edge, relative to the foil center. These results will be used below.

Neglecting stimulated emission, the inverse absorption length is written as

$$\alpha_v^l = \frac{\pi e^2}{m_e c} N_i f_{lu} \varphi(v, v_0),$$

where N_i is the ground state level population for ion i, and $\varphi(v, v_0)$ is the line shape of the absorber.

In order to calculate τ_v, this expression must be integrated through the slab:

$$\tau_v = \int_{-x_0}^{x_0} \alpha_v^l \, dx = \int_{-x_0}^{x_0} \frac{\pi e^2}{m_e c} N_i f_{lu} \varphi(v, v_0) \, dx.$$

Using $u = (u_0/x_0)x$, $dx = (x_0/u_0)\,du$. Assuming a uniform plasma allows N_i to be factored out, giving

$$\tau_v = \frac{\pi e^2}{m_e c} \frac{x_0}{u_0} N_i f_{lu} \int_{-u_0}^{u_0} \varphi(v, v_0) \, du.$$

The absorption line widths in this study are dominated by thermal Doppler broadening. For example, including Stark broadening in the Na He-δ line shape calculation increases its width by

only 5% at $T_i = 150\,\mathrm{eV}$, while the lower series transitions exhibit even smaller Stark broadening. While this additional broadening does affect the line shape in the far wings, the lines are not saturated sufficiently for this to affect their spectrally integrated absorption strength.

Therefore, we approximate the line profile by

$$\varphi(v, v_0) = \frac{1}{\sigma\sqrt{\pi}} \exp\left\{\frac{-[v(1-u/c) - v_0]^2}{\sigma^2}\right\}.$$

Hence,

$$\tau_v = \frac{\pi e^2}{2m_e c} \frac{N_i L f_{lu}}{\sigma\sqrt{\pi} u_0} \int_{-u_0}^{u_0} \exp\left\{\frac{-[v(1-u/c) - v_0]^2}{\sigma^2}\right\} \mathrm{d}u,$$

where $L \equiv 2x_0$ is the width of the plasma. Defining $k_0 = \pi e^2 N_i L f_{lu}/2m_e c$, yields

$$\tau_v = \frac{k_0}{\sigma\sqrt{\pi} u_0} \int_{-u_0}^{u_0} \exp\left\{\frac{-[v(1-u/c) - v_0]^2}{\sigma^2}\right\} \mathrm{d}u.$$

Defining $y = (v - v_0)/\sigma$ and $w = y - vu/v_0 u_{th}$ gives

$$\tau_v = \frac{k_0 v_0 u_{th}}{\sigma v u_0} \int_{y - v u_0/v_0 u_{th}}^{y + v u_0/v_0 u_{th}} \frac{\mathrm{e}^{-w^2}}{\sqrt{\pi}} \mathrm{d}w = \frac{k_0}{2\sigma} \frac{\{\mathrm{erf}(y + vu_0/v_0 u_{th}) - \mathrm{erf}(y - vu_0/v_0 u_{th})\}}{vu_0/v_0 u_{th}}.$$

For these lines, $v/v_0 \approx 1$, giving

$$\tau_v = \frac{k_0 u_{th}}{\sigma u_0} \int_{y - u_0/u_{th}}^{y + u_0/u_{th}} \frac{\mathrm{e}^{-w^2}}{\sqrt{\pi}} \mathrm{d}w = \frac{k_0}{2\sigma} \frac{\{\mathrm{erf}(y + u_0/u_{th}) - \mathrm{erf}(y - u_0/u_{th})\}}{u_0/u_{th}}. \tag{1}$$

This expression reduces to a Gaussian profile having a thermal width σ for the stationary case where $u_0/u_{th} \ll 1$ and flattens to a rectangular function for the case $u_0/u_{th} \gg 1$.

Because the expansion is approximately one-dimensional and the ground-state populations dominate the total population of each ion stage, the areal density summed over each ion stage is conserved and can be written as $\sum_i N_i L = N_0 L_0$, where $N_0 L_0$ is the initial areal density of the solid foil (provided by the manufacturer). Thus, $N_i L = f_i N_0 L_0$, where f_i is the fractional charge state abundance of ion i.

In these experiments the instrumental resolution was insufficient to resolve the line profiles in these relatively low-temperature plasmas. However, the spectrally integrated line strength is independent of the instrumental resolution. Hence we define the measured line absorption strength (equivalent width) as $A = \int\{1 - \exp(-\tau_v)\}\,\mathrm{d}v$, where τ_v is given in Eq. (1). This yields a "curve of growth" relationship, often applied in interpreting astrophysical line strengths [27]

$$\frac{A}{\sigma} = \int \{1 - \exp(-\tau_v)\}\,\mathrm{d}y = \int [1 - \exp\{-\tau_0 g(y)\}]\,\mathrm{d}y, \tag{2}$$

where $\tau_0 = 2k_0/\sqrt{\pi}\sigma$ is the unshifted line-center optical depth, and $g(y)$ is defined through Eq. (1). For optically thin lines where $\tau_0 < 1$, Eq. (2) predicts that the ratio of A/σ is in a linear regime where this ratio is approximately proportional to τ_0. For optically thick lines, A/σ depends on both τ_0 and u_0/u_{th} since the absorption line begins to saturate and broaden. The transition from the linear to the non-linear regime at larger τ_0 is evident in Fig. 3. By fitting a range of data from

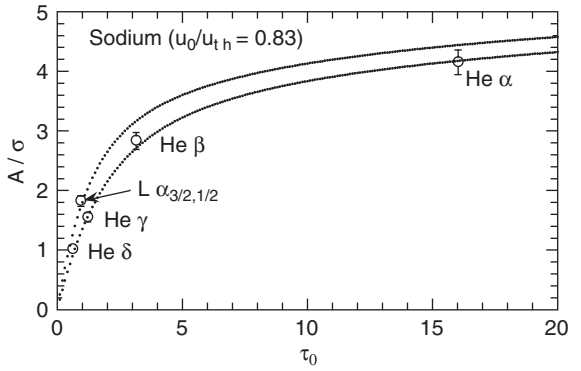

Fig. 3. Curve-of-growth analysis for sodium absorption lines. Vertical error bars assume ±5% uncertainty in the absorption strength determined by numerically integrating the film spectrum for each line. The upper curve was calculated for the blended $Ly\alpha(3/2, 1/2)$ lines separated by 6 mÅ.

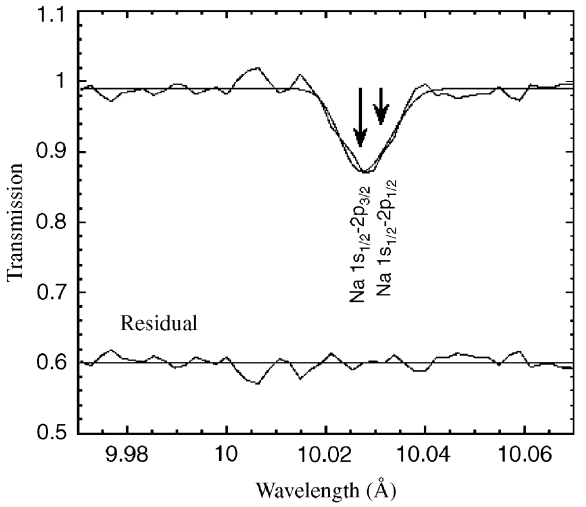

Fig. 4. Na doublet absorption spectrum. The residual curve is offset by 0.6.

relatively weak to strong absorption lines, the relative concentrations of each ion, f_i, can be determined, consistent with the Doppler widths and velocity gradients in the plasma.

In the case when two or more lines are in close proximity, the individual absorption features from each line may be unresolved, due to the resolution of the instrument. If the absorption is weak, the integrated absorption strength will still be the sum of the strengths of each line, even if unresolved. However, if the lines are strongly absorbing, the saturated width of each line may blend into its nearby neighbor. The absorption strength will then depend on both the individual lines strengths as well as the line separations. For example, in the analysis of the L_α Na doublet lines, which are separated by 6 mÅ, the curve of growth is seen to deviate from the single-line curve for $\tau_0 > 1$ (see Fig. 3). The absorption spectra of the blended Na doublet is shown in Fig. 4. The curve of growth derivation for two closely spaced lines is given in Appendix A.

5. Analysis

5.1. Sodium lines

The Na absorption spectra consists of isolated He-like Ryberg series of absorption lines $1s^2 - 1s2p\ (^1S_0^o - {}^1P_1)$, $1s^2 - 1s3p\ (^1S_0^o - {}^1P_1)$, $1s^2 - 1s4p\ (^1S_0^o - {}^1P_1)$, $1s^2 - 1s5p\ (^1S_0^o - {}^1P_1)$, and the H-like $1s - 2p_{1/2,3/2}$ doublet. The absorption strengths for each transition were determined by numerical integration across each line. Fitting a single and a double Gaussian line shape to each transition provided a check for these results. The double Gaussians more accurately included the wings in some of the stronger lines, and typically gave 10−20% higher values in these cases. Uncertainties in the area were determined by the individual uncertainties in the fitting parameters for the line width and height, as obtained from the χ^2 minimization for each line. Relative uncertainties in the τ_0 parameter were set at 5% to include the approximate uncertainties in the oscillator strengths. The Na $1s^2 - 1s2p$ line at 11.003 Å partially overlaps with the Fe^{+16} $2s^22p^6 - 2s2p^64p(^1S_0^o - {}^1P_1)$ line at 11.025 Å, and was analyzed using two shifted double Gaussians (see Fig. 5).

Although neither the ion nor the electron temperatures were measured, a photoionization calculation described below predicts an electron temperature near 150 eV. At this temperature, we estimate that the electron–ion (Fe^{+16}) equilibration time is relatively fast, i.e., ≈ 1 ns [28], and thus we assume that $T_i \approx T_e$ following the peak of the radiation pulse when the charge state distribution is determined. Shown in Fig. 3 is a calculation with $T_i = 150$ eV and $u_0/u_{th} = 0.83$. The data are well fitted by this distribution over a wide range of line strengths. The resulting ratio of Na^{+10}:Na^{+9} (H-like:He-like) ground-state ions is 1:4.5. Note that the determination of the ionization balance depends mostly on the relative absorption strengths of lines from each ion stage, and is relatively insensitive to the ion temperature.

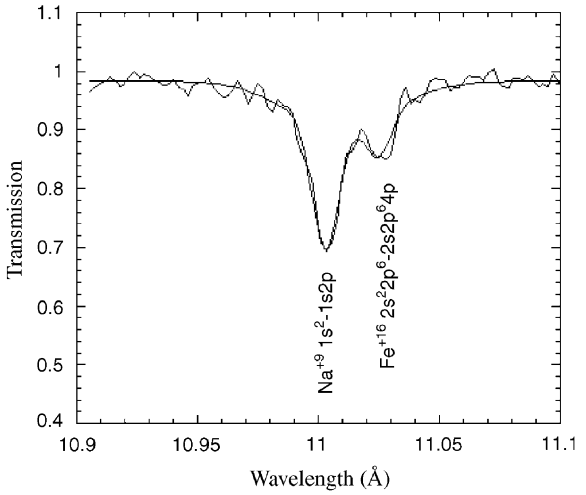

Fig. 5. $Na^{+9}1s^2 - 1s2p$ and the $Fe^{+16}2s - 4p$ absorption lines fit with two double Gaussians.

5.2. Fluorine lines

A similar analysis of F absorption lines was performed using the H-like lines $1s-2p_{1/2,3/2}$, $1s-3p_{1/2,3/2}$, $1s-4p_{1/2,3/2}$, $1s-5p_{1/2,3/2}$, and the He-like $1s^2-1s3p$ ($^1S_0^o-{}^1P_1$), $1s^2-1s4p$ ($^1S_0^o-{}^1P_1$) and $1s^2-1s5p$ ($^1S_0^o-{}^1P_1$) lines. The absorption strengths were obtained by integrating over each line and uncertainties determined from the uncertainties in the fits to the lines. As above, using $T_i = 150\,\text{eV}$ and $u_0/u_{th} = 0.83$, the curve of growth analysis yielded a ratio of 6.0:1 for F^{+8}:F^{+7}. The reversed ratio for F relative to Na is due to its lower photoionization threshold.

5.3. Iron lines

The Fe absorption spectrum was also analyzed using the one-dimensional expansion model described above. Unlike Na and F lines, many Fe absorption features were comprised of multiple unresolved lines, making the curve of growth analysis difficult. Instead, line positions and oscillator strengths were first calculated using the HULLAC suite of codes [29], which generated many thousands of lines. In some cases, line positions were modified to improve agreement with the measured line positions. In case where a few strong lines are closely spaced, such as for Fe^{+17} described below, more accurate line positions from Kelly [30] and Brown et al. [31] were used. The charge state distribution for Fe was determined by varying each charge state concentration, f_i, to best fit the absorption line strengths. Tables 1–4 list the transitions and measured wavelengths for the observed Fe absorption lines. A brief discussion for each ionization stage is given below.

5.3.1. Fe^{+15}

HULLAC calculations of Fe^{+15} transitions yielded 3 bands of lines in the wavelength regions 12.35−12.75 Å ($2s^22p^63s-2s^22p^53s4d$), 13.9−14.1 Å ($2s^22p^63s-2s2p^63s3p$), and 15.1−15.7 Å ($2s^22p^63s-2s^22p^53s3d$). The 15.1−15.7 Å band was predicted to be the strongest, but was spread over a region that blended into the noise of the film, making quantitative analysis difficult. The 13.9−14.1 Å was predicted to be a weaker narrow feature, and was not observed. The first band at 12.35−12.75 Å consisted of 3 subbands that are satellite transitions to the Ne-like ($2s^22p^6-2s^22p^54d$) triplets. The two strongest Na-like satellites, shifted up in wavelength by 0.28 Å, were observed. The absorption strength for these satellite lines were used to determine the relative populations of the Fe^{+15} ion. Due to relatively weak absorption strength and strong line blending, the uncertainty is large. The fractional abundance was found to be $\approx 0.05(\pm 0.03)$.

5.3.2. Fe^{+16}

As shown in Table 1 and Fig. 2, numerous Ne-like Fe absorption lines were identified, such as for transitions $2s^22p^6-2s^2p^5nl, n=3-8, l=s,d$ and $2s^22p^5-2s2p^6np, n=3-5$ transitions. Due to the relatively high abundance of Fe^{+16}, high-n transitions with weak oscillator strengths were observable. The stronger low-n transition lines were saturated but when convolved with the instrumental resolution gave peak fractional absorptions near 0.7−0.8. Using the measured absorption strengths yields a fractional abundance for Fe^{+16} $f_{+16} = 0.8 \pm 0.1$.

Table 1
Fe^{+15} and Fe^{+16} measured absorption lines and wavelengths.

Ion	Transitions	Wavelength (Å)
Fe^{+15}	$2s^22p^63s - 2s^22p^5(P_{1/2})3s4d$ (bands)	12.41
	$2s^22p^63s - 2s^22p^5(P_{3/2})3s4d$ (bands)	12.55
Fe^{+16}	$2s^22p^6 - 2s2p^65p(^1P_1)$	10.128
	$2s^22p^6 - 2s^22p^5(^2P_{1/2})8d$	10.222
	$2s^22p^6 - 2s^22p^5(^2P_{3/2})8d$	10.339
	$2s^22p^6 - 2s^22p^5(^2P_{1/2})7s$	10.440
	$2s^22p^6 - 2s^22p^5(^2P_{3/2})7d$	10.503
	$2s^22p^6 - 2s^22p^5(^2P_{1/2})6d$	10.658
	$2s^22p^6 - 2s^22p^5(^2P_{3/2})6d$	10.772
	$2s^22p^6 - 2s2p^64p(^1P_1)$	11.028
	$2s^22p^6 - 2s^22p^5(^2P_{1/2})5d$	11.131
	$2s^22p^6 - 2s^22p^5(^2P_{3/2})5d$	11.253
	$2s^22p^6 - 2s^22p^5(^2P_{3/2})5s$	11.419
	$2s^22p^6 - 2s^22p^5(^2P_{1/2})4d$	12.122
	$2s^22p^6 - 2s^22p^5(^2P_{3/2})4d$	12.264
	$2s^22p^6 - 2s^22p^5(^2P_{3/2})4d$	12.317
	$2s^22p^6 - 2s^22p^5(^2P_{1/2})4s$	12.525
	$2s^22p^6 - 2s2p^63p(^1P_1)$	13.833
	$2s^22p^6 - 2s2p^63p(^3P_1)$	13.889
	$2s^22p^6 - 2s^22p^5(^2P_{1/2})3d$	15.013
	$2s^22p^6 - 2s^22p^5(^2P_{3/2})3d$	15.262

5.3.3. Fe^{+17}

Measurements of Fe^{+17} absorption lines were used to determine the ionic abundance as well as to investigate the temperature sensitivity of population ratios between the ground state $2s^22p^5(^2P_{3/2})$ and the slightly higher energy level $2s^22p^5(^2P_{1/2})$ at 12.6 eV.

Shown in Fig. 6 are the F-like Fe absorption lines in the region 14.0−14.6 Å. Although not resolved, a total of 21 Fe^{+17} lines in this spectral region were used in the analysis (see Table 2). Both measured [30,31] and calculated line positions and line strengths [29,32] were used to identify line features and determine the relative ground state and upper state populations. The total fractional abundance of Fe^{+17} was found to be $f_{+17} = 0.15 \pm 0.05$, and the ratio of lower to upper populations was 0.5 ± 0.15. This relatively large uncertainty in the ratio is due to the fact that the lines are saturated and therefore, as discussed above, the integrated absorption strengths are not linearly proportional to the populations.

The calculated ratio was then compared to predictions from the collisional-radiative code Flychk (see below), which included a detailed accounting of all relevant atomic process between

Table 2
Absorption lines used in the spectral analysis of Fe^{+17} in the wavelength region 14.0−14.6 Å.

Ion	Transitions	λ^{K}(Å)	λ^{E}(Å)	λ^{H}(Å)	λ^{RM}(Å)	f^{H}	f^{RM}
Fe^{+17}	$2s^22p^5(^2P_{3/2}) - 2s^22p^43d$	(14.120)		14.136	14.144	0.062	0.069
	$2s^22p^5(^2P_{3/2}) - 2s^22p^43d(^2D_{3/2})$	14.150	14.158	14.150	14.163	0.09	0.12
	$2s^22p^5(^2D_{3/2}) - 2s^22p^43d(^2D_{5/2})$	14.202	14.208	14.198	14.213	0.82	0.90
	$2s^22p^5(^2P_{3/2}) - 2s^22p^43d$	(14.204)		14.206	14.218	0.52	0.58
	$2s^22p^5(^2P_{3/2}) - 2s^22p^43d(^2S_{1/2})$	14.255		14.263	14.274	0.19	0.23
	$2s^22p^5(^2P_{3/2}) - 2s^22p^43d$	(14.256)		14.264	14.275	0.04	0.06
	$2s^22p^5(^2P_{3/2}) - 2s^22p^43d(^2D_{5/2})$	14.373	14.373	14.381	14.394	0.28	0.32
	$2s^22p^5(^2P_{3/2}) - 2s^22p^43d$	(14.397)		14.402	14.419	0.01	0.0068
	$2s^22p^5(^2P_{3/2}) - 2s^22p^43d(^2P_{3/2})$	14.419		14.435	14.446	0.03	0.029
	$2s^22p^5(^2P_{3/2}) - 2s^22p^43d(^4D_{3/2})$	14.453		14.465	14.479	0.19	0.23
	$2s^22p^5(^2P_{3/2}) - 2s^22p^43d(^2F_{5/2})$	14.485		14.494	14.510	0.01	0.021
	$2s^22p^5(^2P_{3/2}) - 2s^22p^43d(^2F_{5/2})$	14.536	14.534	14.545	14.558	0.18	0.21
	$2s^22p^5(^2P_{3/2}) - 2s^22p^43d(^4P_{3/2})$	14.551	14.571	14.560	14.575	0.10	0.10
	$2s^22p^5(^2P_{3/2}) - 2s^22p^43d(^4P_{1/2})$	14.581		14.590	14.610	0.04	0.042
	$2s^22p^5(^2P_{1/2}) - 2s^22p^43d(^2D_{3/2})$	14.121		14.076	14.138	0.69	0.86
	$2s^22p^5(^2P_{1/2}) - 2s^22p^43d(^2P_{1/2})$	14.344	14.343	14.341	14.351	0.58	0.66
	$2s^22p^5(^2P_{1/2}) - 2s^22p^43d(^2D_{3/2})$	14.361		14.354	14.371	0.83	0.83
	$2s^22p^5(^2P_{1/2}) - 2s^22p^43d(^4P_{5/2})$	14.419		14.413	14.427	0.16	0.17
	$2s^22p^5(^2P_{1/2}) - 2s^22p^43d(^2S_{1/2})$	14.467		14.472	14.485	0.075	0.088
	$2s^22p^5(^2P_{1/2}) - 2s^22p^43d(^2P_{3/2})$	14.610	14.616	14.615	14.634	0.064	0.067

λ^{K}, λ^{E}, λ^{H}, λ^{RM}, f^{H}, f^{RM} are from Refs. [30,31,29,32,29,32], respectively. Spectral data is fit with wavelengths from λ^{K} and absorption strengths from f^{RM} (see Fig. 6). Wavelengths in parentheses are estimates based on shifted λ^{RM} values and best fit to data.

Table 3
Population ratios of Fe^{+17} levels $2s^22p^5(^2P_{1/2})/2s^22p^5(^2P_{3/2})$.

T_e(eV)	NLTE ratio	LTE ratio
30	0.35	0.33
50	0.39	0.39
70	0.40	0.42
100	0.40	0.44
150	0.41	0.46

each level. The ratios of the $^2P_{1/2}/^2P_{3/2}$ populations as a function of electron temperature are shown in Table 3. Due to its weak sensitivity in this regime, it is not possible to accurately infer an electron temperature. However, this calculation suggests that $T_e > 30$ eV, which is above the

Table 4
Measured Fe^{+18} absorption lines and wavelengths.

Ion	Transitions	Wavelength (Å)
Fe^{+18}	$2s^22p^4 - 2s^22p^34d$	13.393
	$2s^22p^4 - 2s^22p^34d$	13.427
	$2s^22p^4 - 2s^22p^34d$	13.467
	$2s^22p^4 - 2s^22p^34d$	13.650
	$2s2p^5 - 2s2p^43d$	13.669
	$2s^22p^4 - 2s^22p^34s$	14.707

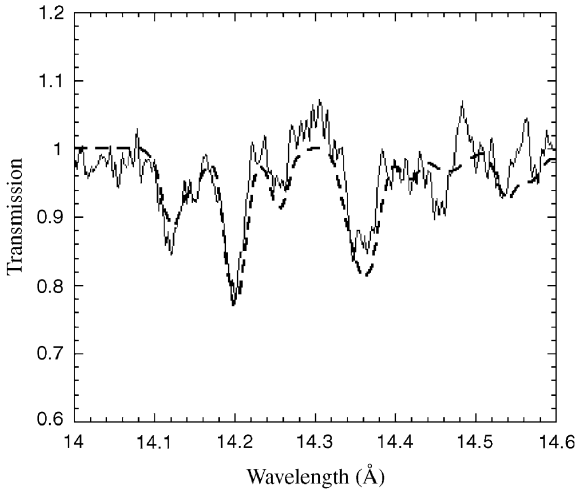

Fig. 6. $Fe^{+17}2s^22p^5 - 2s^22p^43d$ absorption spectrum (solid) and multiple line fit (dashed) used to determine the Fe^{+17} abundance.

regime where 3-body collisional effects "begin to" dominate the ionization balance (see Fig. 7). As discussed below, the photoionization code Cloudy also predicts $T_e \approx 150\,eV$.

5.3.4. Fe^{+18}

Only a few very weak O-like Fe lines were observed. Fe^{+18} lines from transitions $2s^22p^4 - 2s^22p^34d(13.3-13.65\,Å)$, $2s^22p^4 - 2s^22p^34s(14.707\,Å)$, and $2s2p^5 - 2s2p^43d(13.669\,Å)$ were tentatively identified (see Table 4). From this data an upper limit on the fractional abundance of $f_{+18} \leqslant 0.05$ was determined. It is interesting to note that the 13.669 Å absorption line originates from the excited $2s2p^5$ level, which is 157 eV above the ground state. This absorption line might therefore be useful as a temperature diagnostic in a more highly ionized plasma.

5.3.5. Fe charge state distribution

The resulting charge state distribution for Fe is shown in Fig. 7. Uncertainties in the background level and signal to noise of the absorption spectrum were used to estimate the

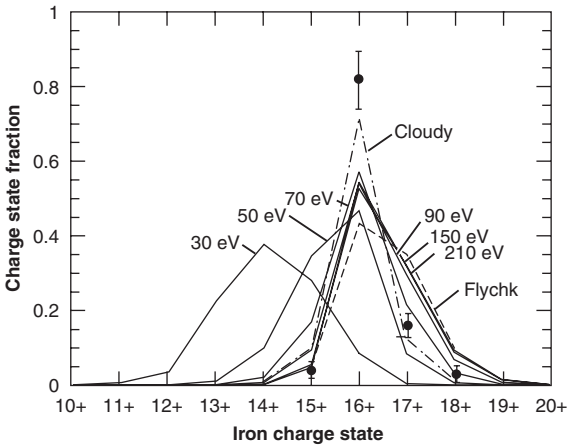

Fig. 7. Measured Fe charge state distribution (solid dots) and comparisons with photoionization code Galaxy for $T_e = 30-210\,\text{eV}$ (solid lines). Also shown are results from the code Flychk at $T_e = 150\,\text{eV}$ (dashed line) and Cloudy (dash–dot). The discrete fractional abundances are connected to aid in viewing.

uncertainties in the charge state populations for each ion. The average charge state for Fe is $\langle Z \rangle = 16.1 \pm 0.2$. Comparisons with various models are discussed below.

5.4. Oxygen

Both O^{+6} and O^{+7} are observed in the absorption spectra, possibly due to the small O component in the plastic tamper and also possibly due to some oxidation of the Fe layer during its manufacture. Therefore, it is difficult to assess the density and temperature of the O. The O^{+6} lines observed were $1s^2 - 1s5p$ (17.396 Å) and $1s^2 - 1s4p$ (17.768 Å). The O^{+7} lines observed were $1s - 5p$ (14.821 Å), $1s - 4p$ (15.176 Å), and $1s - 3p$ (16.006 Å).

6. Photoionization models

The charge state distributions for Fe, Na, and F were calculated using four photoionization codes, Cloudy [6], Galaxy [33], Flychk [34], and Nimp [35]. To simplify the discussion, these codes were run in a steady-state mode at a single temperature and density, i.e., having no spatial variation (0-D). The measured absolute spectral brightness from the pinch is applied as an imbedded isotropic radiation field, using a solid angle calculation between the pinch and the foil. The 0-D modeling implicitly assumes that the continuum radiation is approximately uniform across the plasma. This was verified with a separate 1-D Cloudy calculation that included radiation transport across the plasma [36].

In order to account for the estimated few nanoseconds required to reach steady-state equilibrium [34,37], the values of the absolute spectral flux and sample density ($n_e = 2.0 \pm 0.7 \times 10^{19}\,\text{cm}^{-3}$) used in the calculations were taken at $+3$ ns after the peak of the radiation pulse. The radiation flux decreases slightly during this time ($\leqslant 20\%$) while the density decrease due

to foil expansion is much less. Therefore we estimate that ξ, which depends on their ratio, decreases from 25 to 20 erg cm s^{-1} during this time, which has very small effect on the ionization balance.

6.1. Cloudy

Cloudy [6] is a large-scale spectral synthesis code designed to simulate fully physical conditions within an astrophysical plasma and then predict the emitted spectrum. Cloudy relies on atomic databases to allow accurate comparisons with spectral emission data. Cloudy calculates both the ionization balance and the electron temperature by a detailed energy accounting of all relevant heating and cooling processes in the plasma, such as from collisional excitation followed by radiative cooling. Our first model calculation included a restricted set of Fe emission lines that effectively treated the Fe resonance lines as optically thick. This assumption is consistent with the measured saturation of the strongest Fe lines and the curve of growth plots shown in Fig. 3. This model yielded an electron temperature near $T_e = 150$ eV and an average charge state $\langle Z \rangle \simeq 16.0$, in reasonable agreement with both the measured distribution width and the average ionization state (see Fig. 7). To test the sensitivity to optical depth effects, a second model was constructed which treated all lines as optically thin. This optically thin model yielded a much lower temperature $T_e = 38$ eV, due to enhanced cooling from line emission, and a distribution that peaked at Fe^{+12}. The optically thin approximation is therefore inconsistent with the Fe absorption data and the concomitant change in the state distribution. A more accurate calculation would include a self-consistent treatment of the line transport and population kinetics in an expanding geometry, which is beyond the scope of this work.

6.2. Galaxy

For a given density, temperature, and incident radiation field, Galaxy [33] calculates the steady-state ionization balance within the plasma. Collisional and radiative excitation and ionization, as well as autoionization and all reverse processes, are included. A rate matrix that couples the initial and final levels using simple scaled-hydrogenic expressions is constructed. Accurate Hartree–Dirac–Slater(HDS) cross-sections are used for photoionization out of the ground state of arbitrary ionization stages for elements up to $Z = 30$. For photoionization out of the excited levels, scaled HDS cross-sections are used if the electron being removed is also present in the ground state, and Kramers cross-sections are used otherwise. Corresponding radiative recombination rates are calculated using detailed balance. The Galaxy code employs an average-of-configuration approximation for electronic states with a principal quantum number $n \leqslant 5$ and averages over all the configurations with the same principal quantum number for higher n.

Using these values, the charge state distribution for Fe was calculated for various temperatures between 30 and 210 eV (see Fig. 7). Above 70 eV, the distributions peak near Fe^{+16} and are quite insensitive to the electron temperature. In this temperature regime (90–210 eV) calculations indicate that photoionization of Fe L-shell ions dominates over collisional ionization processes by more than a factor of 10. The weak temperature dependence of the charge-state distribution therefore is likely due to the thermal electrons having insufficient energy to ionize the L-shell ions

in this regime. Below 50 eV, the contribution from three-body recombination begins to dominate, reducing the degree of ionization substantially.

The average charge state predicted by Galaxy in the 90–210 eV temperature range is $\langle Z \rangle \simeq 16.4 \pm 0.2$. The uncertainty in $\langle Z \rangle$ is determined from folding in the uncertainties in the absolute flux (±20%) and density (±35%) measurements. The calculated distribution is slightly more ionized than measured. This may be due, in part, to the fact that the measured time-integrated absorption spectrum is weighted by the time history of the backlighter intensity, which peaks a few nanoseconds before the sample reaches steady-state equilibrium, resulting in a slightly lower average charge. Galaxy calculations of H to He-like ratios for F and Na yielded ratios of 6.7:1 and 1:1.4, respectively at $T_e = 150$ eV. The F ratio agrees well with the data (6.0:1), while the Na data (1:4.5) is substantially less ionized than predicted.

6.3. *Flychk*

Also shown in Fig. 7 are model calculations from the collisional-radiative code Flychk. Energy levels and level populations were calculated using a hydrogenic approximation. Details of the code can be found in Ref. [34]. At $T_e = 150$ eV, Flychk predicts a slightly higher average ionization $\langle Z \rangle \simeq 16.5$. It is interesting to note that Flychk and Galaxy predict broader distributions than Cloudy. For example, for T_e between 70 and 210 eV, Galaxy predicts an average charge that varies between 16.2 and 16.4 and a FWHM that varies between 1.6 and 1.7, much broader than 1.2 for Cloudy. Differences in the widths are likely due to differences in the specific rates that couple the Fe^{+15}, Fe^{+16}, and Fe^{+17} ions.

6.4. *Nimp*

A simple but powerful method for modeling the non-LTE effects in a partially ionized plasma is to treat the distribution of ion stages as a single ion having non-integer electron population in each shell [38]. Rose et al. [35] have developed an average atom model (Nimp) for the purpose of modeling photoionized non-LTE plasmas. All relevant collisional and radiative processes are included. Autoionization and dielectronic recombination rates are calculated for individual principal quantum levels as approximated by Albritton and Wilson [39]. More details about this code can be found in Refs. [33,35]. Calculations and comparisons with data for Fe are shown in Fig. 8 (from Ref. [35]). Also shown are calculations that do not include the radiation field, which clearly illustrates the importance of the X-ray radiation on ionizing the Fe plasma into the L-shell. Excellent agreement for F and Na are also presented in Ref. [35].

7. Summary and discussion

The main goal of these experiments was to produce a strongly photoionized plasma in which the degree of ionization, the density, and radiation flux were independently measured. This work was motivated in part by the recent Chandra and XMM-Newton missions, which are now providing detailed X-ray spectra from strong astrophysical sources, such as AGNs. These experiments were designed to reach an ionization parameter ξ in range of 10–100, which is

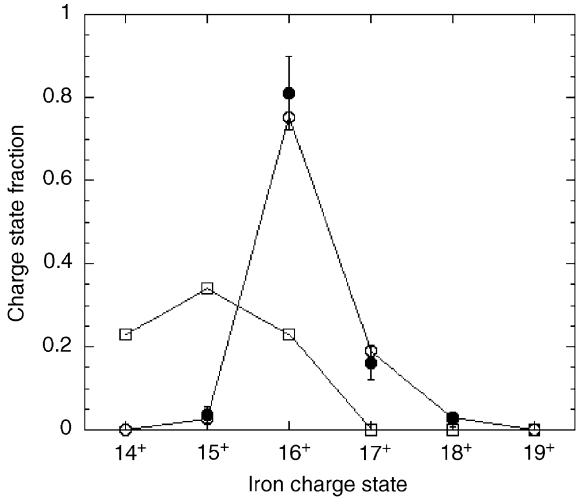

Fig. 8. Measured Fe charge-state distribution (solid dots) and comparisons with the average atom code, Nimp (open dots). Results from Nimp with no radiation field are also shown (open squares) (from Ref. [35]).

relevant to X-ray emission regions near these objects, allowing photoionization codes to be tested in this regime.

Comparisons with four photoionization codes showed reasonable agreement, both with the data and each other. Surprisingly, even the simplest average atom code agreed well with the data. This suggests that such an approach may be sufficient for large-scale modeling, where computer runtime is often hampered by the complexity of the atomic modeling. Simulations with and without the radiation field also directly confirmed that photoionization was the dominant ionization process for these plasmas. More detailed discussion about differences between the codes is beyond the scope of this work, but we hope will be addressed in the future. We also hope these results will stimulate interest in future experiments at the ZR-facility upgrade and at the National Ignition Facility at LLNL, where even higher radiation fluxes are anticipated.

Acknowledgements

The authors thank R.W. Lee for helpful discussions, M.K. Matzen, A.L. Osterheld, and M. Eckart for their support, J. Emig and the Sandia Z-facility team for their technical assistance, and D. L. Fehl for assistance with XRD unfolds. This paper used the photoionization code Cloudy, written by G.J. Ferland, which can be obtained from http://www.nublado.org. This work was performed under the auspices of the US Department of Energy by the University of California Lawrence Livermore National Laboratory under contract No. W-7405-Eng-48. P.v.H. is supported by the Engineering and Physical Sciences Research Council of the United Kingdom. FPK and SJR acknowledge AWE Aldermaston for support through the William Penney Fellowship. This work was also supported by NATO Collaborative Linkage Grant CLG979443.

Appendix A

The absorption profile for two lines with oscillator strengths f_1 and f_2 separated by energy Δv is

$$\tau_v = \frac{k_0}{\sigma\sqrt{\pi}u_0}\int_{-u_0}^{u_0} g_1 \exp\left\{\frac{-[v(1-u/c)-v_0]^2}{\sigma^2}\right\} + g_2 \exp\left\{\frac{-[v(1-u/c)-v_0+\Delta v]^2}{\sigma^2}\right\} \mathrm{d}u,$$

where here $k_0 = \pi e^2 N_i L(f_1+f_2)/2m_e c$ and $g_1 = f_1/(f_1+f_2)$ and $g_2 = f_2/(f_1+f_2)$.

Nothing $u_{th}/c = \sigma/v_0$ and defining $y = (v-v_0)/\sigma$, $w = y - vu/u_{th}v_0$, $z = y - vu/u_{th}v_0 + \Delta v/\sigma$:

$$\tau_v(y) = \frac{k_0 u_{th}}{\sigma u_0}\left\{\int_{y+vu_0/v_0u_{th}}^{y+vu_0/v_0u_{th}} g_1 \frac{\mathrm{e}^{-w^2}}{\sqrt{\pi}}\,\mathrm{d}w + \int_{y-vu_0/v_0u_{th}+\Delta v/\sigma}^{y+vu_0/v_0u_{th}+\Delta v/\sigma} g_2 \frac{\mathrm{e}^{-z^2}}{\sqrt{\pi}}\,\mathrm{d}z\right\}.$$

Integrating and then assuming $v/v_0 \approx 1$ yields

$$\tau_v(y) = \frac{k_0}{2\sigma}\left\{g_1 \frac{\{\mathrm{erf}(y+u_0/u_{th}) - \mathrm{erf}(y-u_0/u_{th})\}}{u_0/u_{th}}\right\}$$
$$+ g_2 \frac{\{\mathrm{erf}(y+u_0/u_{th}+\Delta v/\sigma) - \mathrm{erf}(y-u_0/u_{th}+\Delta v/\sigma)\}}{u_0/u_{th}}\Bigg\}.$$

The curve of growth equation is then

$$\frac{A}{\sigma} = \int\{1-\exp(-\tau_v)\}\,\mathrm{d}y = \int[1-\exp\{-\tau_0 h(y)\}]\,\mathrm{d}y,$$

where $\tau_0 = 2k_0/\sqrt{\pi}\sigma$ is the line-center optical depth of the sum of the line strengths, and $h(y)$ is defined through $\tau_v(y)$. Due to the fact that both A/σ and τ_0 depend on $1/\sigma$, the function is independent of σ and thus T_i, even for the case of doublet lines. For a given line separation and T_i, a family of curves is generated that are only a function of u_0/u_{th}.

References

[1] Paerels F, et al. Ap J 2000;533:L135.
[2] Kaastra JS, Mewe R, Liedahl DA, Brinkman AC, Komossa S. Astr and Astro 2001;354:83.
[3] Netzer H, et al. Ap J 2003;599:933.
[4] Krongold Y, Nicastro F, Brickhouse NS, Elvis M, Liedahl DA, Mathur A. Ap J 2003;597:832.
[5] Netzer H. Ap J 1996;473:781.
[6] Ferland GJ, et al. PASP 1998;110:776.
[7] Netzer H. Ap J 2004;604:551.
[8] Kraemer SB, Ferland GJ, Gabel JR. Ap J 2004;604:556.
[9] Beiersdorfer P, et al. Ap J 1999;519:L185.
[10] Savin DW, et al. AP J 1997;489:L115.
[11] Fournier KB, et al. In: Bautista MA, Kallman TR, Pradhan AK, editors. Workshop on data needs for X-Ray astronomy. Greenbelt, MD: Goddard Space Flight Center; 2000. 9. 127.
[12] Perry TS, et al. Phys Rev E 1996;54:5617.
[13] Springer PT, et al. Phys Rev Lett 1992;69:3735.
[14] Chenais-Popvics C. Laser Particle Beams 2002;20:91 and references therein.
[15] Foord ME, et al. Phys Rev Lett 2000;93:992.
[16] Heeter RF, et al. Phys Rev Lett 2000;93:135.

[17] Morita V, et al. J Quant Spectro Rad 2001;71:519.
[18] Heeter RF, et al. Rev Sci Instr 2001;72:1224.
[19] Foord ME, et al. In: Ferland GJ, Savin DW, editors. Spectroscopic Challenges of Photoionized Plasmas. ASP Conference Series vol. 247, 2001. p. 117.
[20] Bailey JE, et al. Phys Plasmas 2002;9:2186.
[21] Foord ME, et al. Phys Rev Lett 2004;85:055002.
[22] Ruggles LE, et al. Rev Sci Instr 2001;72:1218.
[23] Chandler GA, et al. Rev Sci Instr 1999;70:561.
[24] Sanford TWL, et al. Rev Sci Instr 1997;68:852.
[25] Tarter CB, Tucker WH, Salpeter EE. Ap J 1969;156:94.
[26] Zimmerman G, Kruer WL. Comments Plasma Phys Control Fusion 1975;2:51.
[27] Mihalas D. Stellar astrophysics. San Francisco: Freeman; 1978.
[28] Spitzer L. Physics of fully ionized gases. NY: Interscience; 1956.
[29] Klapisch M, Schwob J, Fraenkel B, Oreg J. J Opt Soc Am 1977;67:148.
[30] Kelly RL. J Phys and Chem Ref Data 1987;16(Suppl. No. 1).
[31] Brown GV, Biersdorfer P, Liedahl DA, Widmann K. Ap J 2005;502:1015.
[32] Jonauskas V., Queen's University, Belfast, RMATRIX calculations, 2004:private communication.
[33] Rose SJ. J Phys B 1998;31:2129.
[34] Chung HK, Morgan WL, Lee RW. J Quant Spect Rad Trans 2003;80:107.
[35] Rose SJ, van Hoof PAM, Jonauskas V, Keenan FP, Kisielius R, Ramsbottom C, Foord ME, Heeter RF, Springer PT. J Phys B 2004;37:L337–42.
[36] van Hoof PAM. One-dimensional cloudy simulations, 2004, Queen's University, Belfast, private communication.
[37] Chung HK. Time-dependent Flychk simulations, 2003, Lawrence Livermore National Laboratory, private communication.
[38] Grasberger WH, Lawrence Livermore National Laboratory Internal Report UCRL-12408 (1965).
[39] Albritton JR, Wilson BG. Phys Rev Lett 1999;83:1594.